UNSTEADY AERODYNAMICS OF THE SAGITTA FLYING WING CONFIGURATION

S. Pfnür, C. Breitsamter

Chair of Aerodynamics and Fluid Mechanics
Technical University of Munich
Boltzmannstr. 15, 85748 Garching

Abstract

The dynamic damping derivatives associated with the pitching and yawing motion of the SAGITTA flying wing configuration at low Mach number conditions are presented. A tailless variant of the configuration and a variant with attached double vertical tail are investigated. The damping derivatives are determined by means of the response of aerodynamic forces and moments to forced harmonic oscillations. The required data for the determination of the damping derivatives is obtained from time-accurate Reynolds-Averaged Navier-Stokes computations. The calculation methodology for the pitch- and yaw-damping derivatives for arbitrary freestream conditions is described and a short evaluation of the approach is presented. Angle of attack and sideslip angle trends as well as the effect of the double vertical tail on the dynamic stability are investigated. For moderate freestream conditions the damping derivatives exhibit an almost constant distribution with respect to the angle of attack and the sideslip angle. With increasing angle of attack and sideslip angle, however, significant non-linear characteristics are observed. The pitch-damping derivatives indicate a dynamically stable behavior for both configurations and all freestream conditions. In contrast, the lateral damping characteristics are much more critical. Both configurations exhibit unstable behavior at several freestream conditions. The vertical tail considerably increases the lateral dynamic stability of the SAGITTA configuration.

NOMENCLATURE

AR	Wing aspect ratio
b	Wingspan, [m]
C_v	Arbitrary aerodynamic coefficient
$C_{v\zeta}$	Arbitrary steady derivative
$C_{v\dot\zeta}$	Arbitrary dynamic derivative
C_{mx}	Rolling moment coefficient, $= M_x/(\rho_\infty/2 U_\infty^2 S_{ref}s)$
$C_{mx\beta}$	Rolling moment derivative, $= dC_{mx}/d\beta$
C_{my}	Pitching moment coefficient, $= M_y/(\rho_\infty/2 U_\infty^2 S_{ref}l_\mu)$
$C_{my\alpha}$	Pitching moment derivative, $= dC_{my}/d\alpha$
$C_{my\dot\alpha} + C_{myq}$	Pitch-damping derivative
C_{mz}	Yawing moment coefficient, $= M_z/(\rho_\infty/2 U_\infty^2 S_{ref}s)$
$C_{mz\beta}$	Yawing moment derivative, $= dC_{mz}/d\beta$
$C_{mzr} - C_{mz\dot\beta}$	Yaw-damping derivative
c_r	Root chord length, [m]
c_t	Tip chord length, [m]
f	Frequency, [Hz]
g	Prism layer stretching factor
h_1	Initial prism layer thickness, [m]
k	Reduced frequency
l_μ	Mean aerodynamic chord, [m]
Ma	Mach number
M_x	Rolling moment, [Nm]
M_y	Pitching moment, [Nm]
M_z	Yawing moment, [Nm]
p	Roll rate, [rad/s]
q	Pitch rate, [rad/s]
r	Yaw rate, [rad/s]
Re	Reynolds number
S_{ref}	Reference area, [m^2]
s	wing semi span, [m]
T	Temperature, [K]
t	Physical time, [s]

U_∞	Freestream velocity [m/s]
x_{mrp}	Moment reference point, [m]
x, y, z	Cartesian coordinates, [m]
y^+	Dimensionless wall distance
α	Angle of attack, [deg]
β	Sideslip angle, [deg]
λ	Wing taper ratio
φ_{le}	Leading-edge sweep, [deg]
φ_{te}	Trailing-edge sweep, [deg]
ρ_∞	Freestream density, [kg/m^3]
ζ	Arbitrary degree of freedom
Ψ	Yaw angle, [rad]
Θ	Pitch angle, [rad]
τ	Dimensionless time
ω	Angular velocity, [rad/s]

Subscripts

b	Body fixed
g	Geodesic
j	j-th harmonic
max	Maximum
0	Initial

Superscripts

~	Harmonic

1. INTRODUCTION

The flow around wings with moderate to high leading-edge sweep angle and small wing aspect ratio are characterized by leading-edge vortices, which already evolve at low angles of attack. In the recent decades mainly slender delta wings with sharp leading edges have been investigated. The formation of the leading edge vortices at these configurations has been extensively studied and the

corresponding flow physics are well understood to a large extent and are well documented [1,2,3].

In recent years the focus was on configurations with reduced wing sweep and (partial) rounded leading edge contours. Investigations on diamond-wing configurations with moderate wing sweep and (partial) rounded leading edge contours concentrate on the vortex formation and control efficiency [4,5,6,7]. Considering the SAGITTA configuration, a comprehensive data set with respect to steady aerodynamic characteristics was obtained in the context of these investigations. The unsteady/dynamic aerodynamic characteristics of such a configuration have not been subject to detailed investigations. A flying wing configuration with a lambda like wing planform was investigated in more detail, whereas this configuration features considerable complex aerodynamic characteristics [8,9]. This article focuses on the unsteady aerodynamic characteristics of the SAGITTA diamond-wing configuration. Although the steady aerodynamics of the SAGITTA configuration does not feature significant non-linear characteristics, the unsteady aerodynamics of this configuration require a detailed investigation.

In the linearized form of the flight mechanics equations of motion the aerodynamic forces and moments are expressed via coefficients and derivatives [10]. The derivatives can be distinguished in the static, dynamic and control derivatives [11]. The dynamic derivatives are necessary in order to describe the behavior of the aircraft in consequence of unsteady aircraft motions and unsteady freestream conditions. Knowledge about the dynamic derivatives is especially important for high angles of attack, where strong non-linear characteristics are expected [12]. They can be obtained from flight testing, wind tunnel testing, CFD computations or a combined approach using data sheets, linear aerodynamic theory and empirical relations [13]. A typical approach for determining the dynamic derivatives uses the response of the aerodynamic forces and moments to forced harmonic oscillations [9,14,15]. The dynamic derivatives are calculated by processing the resulting temporal aerodynamic force and moment distributions. Different approaches based on linear [16] and non-linear assumptions [17] exist. There are different forms of oscillating motions. The oscillations can be performed as a rotary motion about a body fixed axis or an oscillating motion along a defined axis or a combination of both, see Ref. [15]. The oscillating motions presented in this article are of rotary kind about a body-fixed axis. The resulting dynamic derivatives can be assigned as damping derivatives, cross derivatives and cross-coupling derivatives [15]. This article deals with the damping derivatives associated with the pitching and yawing motion.

2. SAGITTA DIAMOND WING CONFIGURATION

The presented investigations are performed on the SAGITTA flying wing configuration. The SAGITTA configuration is of diamond wing planform type and features a positive leading-edge sweep angle of $\varphi_{le} = 55°$ and a negative trailing-edge sweep angle of $\varphi_{te} = -25°$. The wing aspect ratio results in AR = 2.010 and the wing taper ratio in $\lambda = 0.025$. In accordance with former wind tunnel investigations on the SAGITTA diamond-wing configuration at the Chair of Aerodynamics and Fluid Mechanics of the Technical University of Munich (TUM-AER) [7] a root chord length of $c_r = 1$ m corresponding to the root chord length of the applied wind tunnel model is chosen. The SAGITTA wind tunnel model represents a 1:12-scaled model of the SAGITTA configuration defined by Airbus Defence and Space [18]. The model configuration exhibits a wing span of b = 1.029 m, a tip chord length of $c_t = 0.025$ m, a mean aerodynamic chord of $l_\mu = 0.667$ m, a moment reference point of $x_{mrp} = 0.418 \cdot c_r$ and a reference area of $S_{ref} = 0.528$ m^2. The wing planform properties are additionally summarized in Figure 1 and Table 1. The SAGITTA configuration features a symmetric NACA 64A0012 airfoil with twelve percent relative thickness over the whole wing span, whereas the airfoil is slightly modified at the inboard wing section. Within the first twenty percent of the wing half span the blunt leading edge is replaced by a sharp leading edge. In consequence of the sharp leading edge at the wing inboard section, a geometrically predefined flow separation already takes place at moderate angles of attack. The separated flow in the inboard section rolls up and leads to a vortex formation near the wing surface [3]. In order to increase the lateral stability of the configuration, a double vertical tail is attached for the first flight campaign of the 1:4-scaled SAGITTA demonstrator, see Figure 2. Due to low-observability reasons, the final SAGITTA configuration will be not equipped with vertical tails. Stability and controllability must therefore be ensured by means of the equipped control devices. Both, the SAGITTA configuration with (SG-VT) and without the attached double vertical tail (SG-00) are considered in the present numerical investigation on the 1:12-scaled W/T model geometry.

c_r	[m]	1	φ_{te}	[°]	-25
c_t	[m]	0.025	λ	[-]	0.025
b	[m]	1.029	AR	[-]	2.010
S_{ref}	[m^2]	0.528	l_μ	[m]	0.667
φ_{le}	[°]	55	x_{mrp}	[m]	0.418·c_r

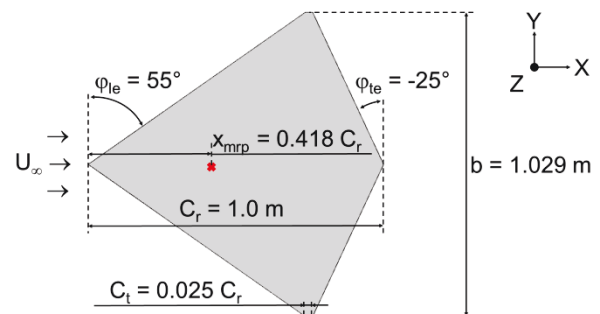TAB 1. Wing planform parameters of the SAGITTA diamond-wing configuration.

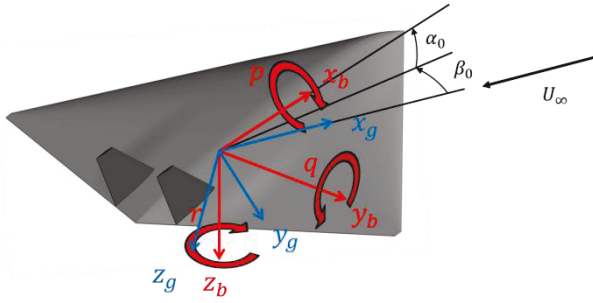FIG 1. Geometric details of the SAGITTA diamond-wing configuration.

FIG 2.   SAGITTA diamond-wing configuration inclusive geodesic (g) and body-fixed (b) coordinate system.

3.   CALCULATION METHODOLOGY OF THE DYNAMIC DERIVATIVES

The dynamic derivatives are determined by means of the aerodynamic response to forced harmonic rigid body motions. The considered types of body motion are the pitching and yawing motion, see Figure 3a and Figure 3b. The pitching motion is a rotation of the SAGITTA diamond wing about the body fixed y-axis and the yawing motion is a rotation about the body fixed z-axis. The center of rotation is the moment reference point x_{mrp}. The applied body-fixed coordinate system with positive rotation directions is highlighted in Figure 2. The body fixed coordinate system is indicated by the subscript letter b.

The forced harmonic oscillations of the rigid body result in a harmonic response of the aerodynamic forces and moments. The harmonic response features the same frequency as the harmonic motion but incorporates a certain phase shift relative to the harmonic motion. The phase shift between the excitation and the aerodynamic response arises due to the dynamic effects of the rigid body motion. It can be exploited in order to determine the dynamic characteristics of the aircraft.

The approach used to calculate the dynamic derivatives from the aerodynamic response to a forced harmonic oscillation is based on the expression of an aerodynamic coefficient as a Taylor series expansion:

$$(1) \quad C_\nu(k\tau) = C_{\nu 0} + C_{\nu\zeta} \cdot \zeta(k\tau) + C_{\nu\dot\zeta} \cdot \dot\zeta(k\tau) + \cdots$$

The subscript ν denotes an arbitrary aerodynamic force or moment coefficient and ζ denotes the degree of freedom like the angle of attack α. k is the reduced frequency and τ the non-dimensional time. They are defined as

$$(2) \quad k = \frac{\omega \cdot l_\mu}{U_\infty}, \ \tau = \frac{t \cdot U_\infty}{l_\mu}.$$

This approach assumes linear characteristics of the aerodynamic coefficients C_ν with respect to the degree of freedom ζ and its temporal derivative. The relation of the aerodynamic coefficient expressed by a Taylor series expansion and the harmonic aerodynamic response is presented in the following paragraph, cf. Ref. [15].

The harmonic oscillation and its derivative can be expressed by

$$(3) \quad \zeta(k\tau) = \zeta_0 + \zeta_{max}\sin(k\tau), \qquad \dot\zeta(k\tau) = \zeta_{max}k\cos(k\tau).$$

Since $\zeta(k\tau)$ is a 2π-periodic function, the derivatives can be determined by a harmonic analysis. $C_\nu(k\tau)$ can then be expressed by a complex amplitude $\tilde{C}_{\nu j}$ and the complex oscillation $e^{ik\tau}$:

$$(4) \quad C_\nu(k\tau) = \bar{C}_\nu + \sum_{j=1}^{n} \text{Re}\big[\tilde{C}_{\nu j} e^{ijk\tau}\big].$$

Applying Euler's identity on Equation (4) and neglecting terms of higher order as well as the imaginary part leads to

$$(5) \quad C_\nu(k\tau) = \bar{C}_\nu + \text{Re}\big[\tilde{C}_{\nu 1}\big]\cos(k\tau) - \text{Im}\big[\tilde{C}_{\nu 1}\big]\sin(k\tau).$$

Replacing Equation (3) by its harmonic expressions

$$(6) \quad \zeta(k\tau) = \zeta_0 + \zeta_{max}e^{ik\tau}, \ \dot\zeta(k\tau) = ik\zeta_{max}e^{ik\tau},$$

substituting them in Equation (1) and only considering the real part results in

$$(7) \quad C_\nu(k\tau) = C_{\nu 0} + (\zeta_0 + \zeta_{max}\cos(k\tau))C_{\nu\zeta} - C_{\nu\dot\zeta}\zeta_{max}k\sin(k\tau).$$

Comparing the coefficients of Equation (7) and Equation (5) gives the relations for the aerodynamic derivatives:

$$(8) \quad C_{\nu\zeta} = \frac{\text{Re}[\tilde{C}_{\nu 1}]}{\zeta_{max}} \qquad C_{\nu\dot\zeta} = \frac{\text{Im}[\tilde{C}_{\nu 1}]}{k\zeta_{max}}$$

3.1.   Pitching Motion

In Equation (1) it is assumed that the coefficient C_ν only depends on one degree of freedom. The pitch oscillation about the body fixed axis, however, represents a combination of two degrees of freedom, namely the angle of attack α and the pitch rate q. The Taylor series expansion of the pitching motion reads

$$(9) \quad C_\nu(k\tau) = C_{\nu 0} + C_{\nu\alpha}\alpha(k\tau) + C_{\nu\dot\alpha}\dot\alpha(k\tau) + C_{\nu q}q(k\tau) + C_{\nu\dot q}\dot q(k\tau).$$

The last term in Equation (9) is often omitted, because $\dot q$ is proportional to $\ddot\alpha$. Equation (9) can then be rewritten as

$$(10) \quad C_\nu(k\tau) = C_{\nu 0} + C_{\nu\alpha}\alpha(k\tau) + \big(C_{\nu\dot\alpha} + C_{\nu q}\big)\dot\alpha(k\tau).$$

Consequently, the pitching oscillation delivers the combination of two derivatives. For an arbitrary freestream condition considering $\alpha_0 \neq 0°$ and $\beta_0 \neq 0°$, Equation (10) must be expanded to

$$(11) \quad C_\nu(k\tau) = C_{\nu 0} + C_{\nu\beta}\beta(k\tau) + C_{\nu\alpha}\alpha(k\tau) + \big(C_{\nu\dot\alpha} + C_{\nu q}\big)\dot\alpha(k\tau).$$

The angle of attack α and the sideslip angle β are defined as

$$(12) \quad \alpha(k\tau) = \alpha_0 + \Theta_{max}e^{ik\tau}; \ \beta(k\tau) = \beta_0,$$

with Θ being the pitch amplitude. Substituting Equation (12) in Equation (11) and performing the coefficient comparison with Equation (5) results in

$$(13) \quad C_{\nu\alpha} = \frac{\text{Re}[\tilde{C}_{\nu 1}]}{\Theta_{max}}; \ C_{\nu\dot\alpha} + C_{\nu q} = \frac{\text{Im}[\tilde{C}_{\nu 1}]}{k\Theta_{max}}.$$

3.2.   Yawing Motion

The yawing motion is a combination of two degrees of freedom, namely the sideslip angle β and the yaw rate r. The corresponding Taylor series expansion reads

$$(14) \quad C_\nu(k\tau) = C_{\nu 0} + C_{\nu\beta}\beta(k\tau) + C_{\nu\dot\beta}\dot\beta(k\tau) + C_{\nu r}r(k\tau) + C_{\nu\dot r}\dot r(k\tau).$$

Since the yawing angular velocity $\dot\Psi$ is proportional to the yaw rate r, the Taylor expansion can be rewritten as

$$(15) \quad C_\nu(k\tau) = C_{\nu 0} + C_{\nu\beta}\beta(k\tau) + C_{\nu\dot\beta}\dot\beta(k\tau) + C_{\nu r}\dot\Psi(k\tau).$$
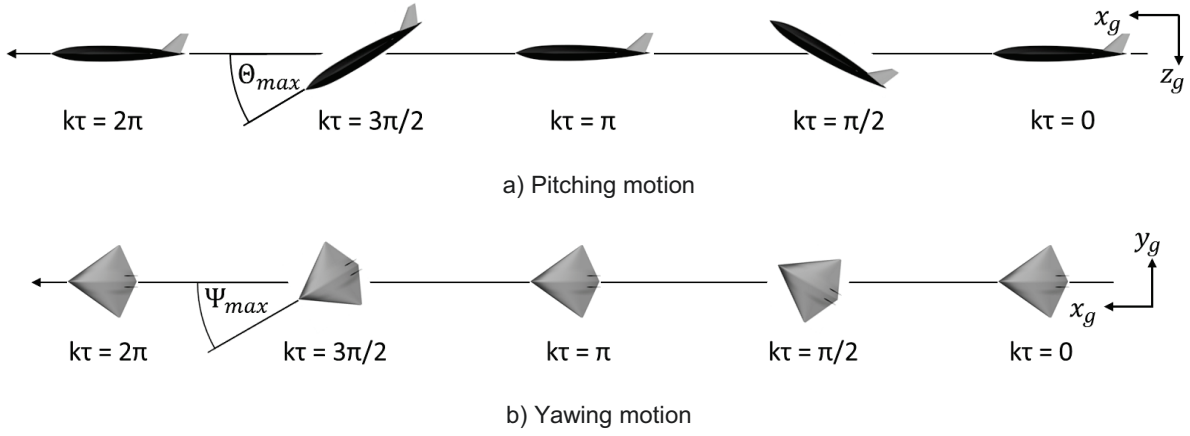
a) Pitching motion

b) Yawing motion

FIG 3.   Applied forced harmonic rigid body motion.

In order to account for initial freestream conditions deviating from $\alpha_0 = 0°$ and $\beta_0 = 0°$, Equation (15) is expanded to

(16) $C_v(k\tau) = C_{v0} + C_{v\alpha}\alpha(k\tau) + C_{v\beta}\beta(k\tau) + C_{v\dot\beta}\dot\beta(k\tau) + C_{vr}\Psi(k\tau).$

For an arbitrary initial freestream condition the effective angle of attack in consequence of the yaw motion about the body fixed z-axis changes in time. It can be approximated as

(17) $\sin\alpha(k\tau) =$
$\cos\Psi(k\tau)\sin\alpha_0 +$
$\cos\beta_0\sin\alpha_0\sin\Psi(k\tau)(\cos\beta_0\sin\Psi(k\tau) - \cos\alpha_0\cos\Psi(k\tau)\sin\beta_0).$

Considering a yaw motion with $\Psi_{max} = 1°$ at a freestream condition of $\alpha_0 = 16°$ and $\beta_0 = 8°$ results in a maximum induced angle of attack of $\Delta\alpha_{max} = 0.03557°$, which can be neglected. Consequently, the angle of attack is written as

(18) $\alpha(k\tau) \approx \alpha_0.$

The effective sideslip angle β is calculated by

(19) $\sin\beta(k\tau) = \cos\Psi(k\tau)\sin\beta_0 - \cos\alpha_0\cos\beta_0\sin\Psi(k\tau).$

Applying the small angle approximation on β and Ψ the sideslip angle and its derivative result in

(20) $\beta(k\tau) = \beta_0 - \Psi(k\tau)\cos\alpha_0,$

(21) $\dot\beta(k\tau) = -\dot\Psi(k\tau)\cos\alpha_0.$

The Taylor expansion finally results in

(22) $C_v(k\tau) = C_{v0} + C_{v\alpha}\alpha_0 + C_{v\beta}(\beta_0 - \Psi(k\tau)\cos\alpha_0) + (C_{vr} - C_{v\dot\beta}\cos\alpha_0)\Psi(k\tau).$

Applying the harmonic oscillation $\Psi(k\tau) = \Psi_{max}e^{ik\tau}$, results in the following expressions for the aerodynamic derivatives.

(23) $C_{v\beta} = -\dfrac{\mathrm{Re}[\tilde{C}_{v1}]}{\Psi_{max}\cos\alpha_0}; \; C_{vr} - C_{v\dot\beta}\cos\alpha_0 = \dfrac{\mathrm{Im}[\tilde{C}_{v1}]}{k\Psi_{max}}.$

4.   NUMERICAL APPROACH

4.1.   Grid Generation

The applied numerical grids are of hybrid unstructured type. They are generated with the grid generation software CENTAUR[1]. The wing surface is meshed with unstructured surface elements of triangular and/or quadrilateral type. Based on the unstructured surface mesh, a quasi-structured prismatic grid is created by a wall normal extrusion of the surface elements. The remaining domain is filled with tetrahedral elements.

In line with former numerical investigations of the SAGITTA configuration, the surface mesh is considerably refined towards the wing leading edge [4], see Figure 4. Since the prismatic grid needs to resolve the boundary-layer flow, certain requirements need to be fulfilled in order to ensure a high quality grid in the vicinity of the wing surface. The first cell height of the prismatic grid is set to $h_1 \approx 0.004$ mm, which leads to a maximum y^+-level of $y^+_{max} \approx 1$, see Figure 5. This ensures a proper resolution of the viscous sublayer of the boundary-layer flow. Overall, the prismatic grid is composed of 38 prism layers. The wall normal stretching factor is set to $g = 1.235$ for the first 30 prism layers. The remaining prism layers feature a constant cell height due to a stretching factor of $g = 1$. The remaining domain is filled with tetrahedral elements. The tetrahedral elements are considerably refined in the vicinity of the upper wing surface in order to provide a well resolved grid for the separated vortex flow structures.
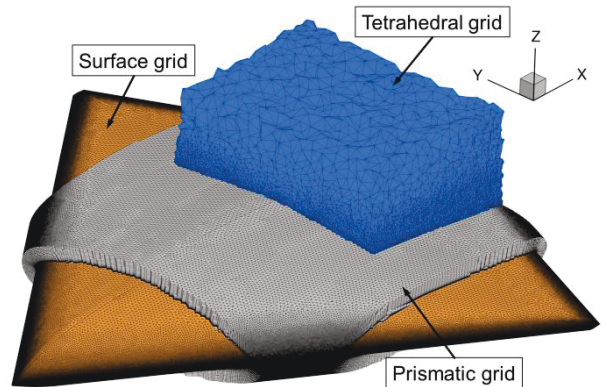

FIG 4.   Numerical grid of the SG-00 configuration.
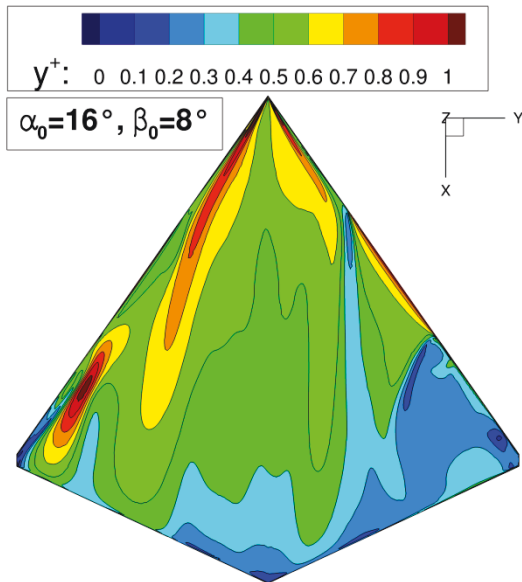
---

[1] https://www.centaursoft.com, retrieved July 2016.

FIG 5. y^+-distribution of the SG-00 configuration for $\alpha_0 = 16°$ and $\beta_0 = 8°$.

The computational domain is restricted by a sphere with a radius of 20 semi wing spans. The overall grid of the SAGITTA configuration with double V/T consists of $23 \cdot 10^6$ grid nodes. The configuration without double V/T features $14 \cdot 10^6$ grid nodes.

4.2. Flow Solver

The simulations presented in this article are performed with the TAU-Code, a CFD solver developed by the German Aerospace Center (DLR) Institute of Aerodynamics and Flow Technology [19]. The TAU-Code is able to solve the three-dimensional compressible (unsteady) Reynolds-Averaged Navier-Stokes (U)RANS equations. It is optimized for the usage with hybrid unstructured grids and developed with respect to parallel efficiency on high-performance computers. The CFD code uses a finite volume scheme and is based on a dual grid approach [20]. The TAU-Code is composed of several modules, which can be executed independently. The most important modules are the preprocessing and solver module.

During the preprocessing, the secondary grid required for the dual grid approach is generated. It is computed according to the cell vertex grid metric from the initial primary grid. Furthermore, the additional coarser grids for the multigrid approach are created during the preprocessing.

The solver module solves the (U)RANS equations on the provided dual grid. Several upwind and central schemes are implemented for the finite volume discretization. Depending on steady-state or time-accurate simulations, local, dual, or global time stepping schemes are available. Multigrid and residual smoothing algorithms are implemented in order to accelerate the convergence of the solution. Turbulent flows can be modelled with several one- and two-equation eddy-viscosity models such as the Spalart-Allmaras (SA) or Menter-SST model, as well as with different kinds of Reynolds stress models [19].

4.3. Numerical Set-up and Test Conditions

The DLR TAU-Code has already been validated for low-aspect-ratio configurations with vortex dominated flow and (partial) rounded leading edges. This experience is utilized for the numerical set-up of the present configuration [4,8,21].

For the spatial discretization, a second order central scheme introduced by Jameson is applied [22]. A matrix-valued coefficient adds the necessary artificial viscosity. By using the matrix dissipation scheme, central difference schemes become closer to upwind biased methods [23]. The temporal discretization is realized by an implicit backwards Euler method with a LUSGS algorithm [24] and a dual time stepping scheme. A three-level 3w multigrid cycle and a point-explicit residual smoother are used in order to accelerate the convergence of the solution. For turbulence modelling of the fully-turbulent simulations, the one-equation SA eddy viscosity model is applied [25]. However, the modified SA-neg version is applied, which is able to cope with negative values of the SA viscosity without any negative influence on the numerical solution [26]. For comparable configurations, the SA model showed good accordance to experimental results in former investigations. Especially, in predicting the pitching moment coefficient at higher angles of attack it was superior to compared two-equation models [8,27]. The oscillating motions are realized by means of the rigid body motion module of the TAU-Code.

Periodic motions are described as a combination of polynomial and Fourier series. The mathematical description of a rotational motion reads

$$\Phi(t) = \sum_{n=0}^{n=N_{PR}} r_n t^n + c_0 + \sum_{n=1}^{n=N_{FR}} (c_n \cos(n\omega t) + d_n \sin(n\omega t))$$

Φ denotes a rotation angle about a body fixed axis, ω denotes the angular velocity and r, c, d denote the coefficients. The desired periodic motion can be realized by an according definition of the polynomial and Fourier coefficients. After the simulation of one period, a standard Fourier analysis is applied to the history of aerodynamic coefficients by the solver. This results in the harmonics of the aerodynamic coefficients. One periodic body motion is performed by 100 physical time steps. Depending on the freestream condition, the number of inner iterations per time step is set to 1000 or 1500, and the number of simulated periods varies between two and three.

All simulations are performed at low Mach number conditions, which are comparable to the wind tunnel conditions of former steady experimental investigations. This enables a comparison of the steady numerical results with the steady experimental data. The analyses are performed for a Mach number of $Ma_\infty = 0.12$ and a Reynolds number of $Re_\infty = 1.7 \cdot 10^6$ based on a mean aerodynamic chord of $l_\mu = 0.667$ m. With a reference temperature of $T_\infty = 288.15$ K this results in a freestream velocity of $U_\infty = 40.83$ m/s. The considered initial angles of attack are $\alpha_0 = \{0°, 4°, 8°, 12°, 16°\}$ and the initial sideslip angles are $\beta_0 = 0°$, $\beta_0 = 4°$, and $\beta_0 = 8°$. Due to the symmetric configuration, only positive sideslip angles are investigated. The harmonic oscillations are performed for a reduced frequency of k = 0.1 (f = 0.974 Hz) and with maximum excitation amplitudes of $\Theta_{max} = \Psi_{max} = 1°$. The rotations have been performed about the moment reference point x_{mrp}, see Table 1 and Figure 1.

All simulations have been run in parallel mode at the GCS

Supercomputer SuperMUC at the Leibniz Supercomputing Centre (LRZ).

5. RESULTS AND DISCUSSION

5.1. Evaluation of the Approach

The evaluation is necessary, as the applied approach is related to some restrictions, e.g. linear characteristics of the aerodynamic coefficients with respect to the degree of freedom ζ and the reduced frequency k. In order to obtain information about the applicability of the method, steady aerodynamic derivatives, Lissajous figures and a variation of the reduced frequency is considered. The SG-VT configuration is used for this purpose.

The steady aerodynamic derivatives obtained from the dynamic simulations, see Equation (8), are compared to the steady aerodynamic derivatives obtained from steady numerical simulations and steady wind tunnel tests. The experimental data is available from former wind tunnel tests. The corresponding wind tunnel model and the results are presented in Ref. [7]. Figure 6 illustrates some steady aerodynamic derivatives obtained from the dynamic numerical simulations (Dynamic CFD), from the steady numerical simulations (Steady CFD) and from the steady wind tunnel tests (Steady W/T). In this way the plausibility of the approach can be checked.

Figure 6a shows the pitching moment derivative versus the angle of attack for $\beta_0 = 0°$ for the three different data sources. Considering the dynamic motion, the pitching moment derivative is obtained by Equation (13). The pitching moment derivatives resulting from the steady motions are obtained by linear interpolation around the discrete data points. Only a small deviation between the numerical and the experimental results is visible. The reason for this deviation is discussed in Ref. [7]. The numerical results, however, show good agreement. Only small deviations are observed for angles of attack of $\alpha_0 \geq 8°$.

The rolling moment coefficient versus the angle of attack for $\beta_0 = 8°$ is shown in Figure 6b. The yawing motion allows the determination of the rolling moment derivative via Equation (23). All three sources show good agreement up to an angle of attack of $\alpha_0 = 12°$. Slight deviations are visible at $\alpha_0 = 16°$. The yawing moment derivative is also shown for a sideslip angle of $\beta_0 = 8°$. It exhibits deviations between all data sources over the whole considered angle of attack range, see Figure 6c. Comparing the yawing moment derivatives obtained from the numerical data sources with the derivatives obtained from the experimental data, shows acceptable deviations. The presented results substantiate the application of the previously described approach for calculating the dynamic derivatives.

In addition, the absence of higher harmonics and non-linearities needs to be checked since they are neglected in the applied approach. In order to avoid higher harmonics in the aerodynamic response, moderate excitation amplitudes of $\Psi_{max} = \Theta_{max} = 1°$ and a moderate reduced frequency of k = 0.1 are used for the harmonic motions. Figure 7 shows the Lissajous figures for selected freestream conditions and aerodynamic coefficients. On the one hand, it shows the Lissajous figures obtained from the temporal distribution of the aerodynamic coefficient (marked as "Temporal"). On the other hand, it shows the Lissajous figures for the reconstructed temporal distribution of the aerodynamic coefficient from the first harmonic of the corresponding aerodynamic coefficient (marked as "1. Harmonic"), see Equation (5).

Figure 7a presents the Lissajous figure of the pitching moment coefficient for $\alpha_0 = 0°$ and $\beta_0 = 0°$. For this flight condition, the assumed absence of higher harmonics and linear characteristics are clearly confirmed. Figure 7b, however, illustrates the Lissajous figure of the pitching moment coefficient for $\alpha_0 = 16°$ and $\beta_0 = 8°$. Although non-linear characteristics could be expected for such freestream conditions, the moderate reduced frequency and excitation angle results in almost linear characteristics without higher harmonics. Slight deviations between the Temporal and the 1. Harmonic curve indicate small non-linear effects. Those non-linear effects are very weak and can thus be neglected. Considering the yawing motion, the Lissajous figure of the yawing moment coefficient is depicted, see Figure 7c. The Lissajous figure represents a freestream condition of $\alpha_0 = 16°$ and $\beta_0 = 8°$. Once again, the linearity and the absence of higher harmonics can be observed. In the vicinity of the maximum positive excitation, slight non-linear effects can be observed.
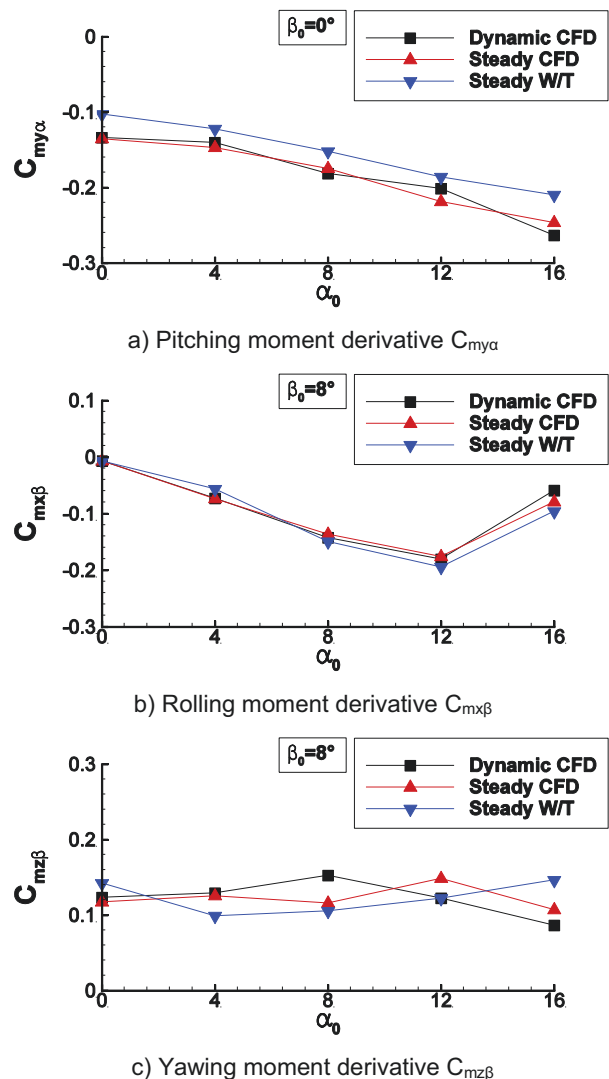

a) Pitching moment derivative $C_{my\alpha}$

b) Rolling moment derivative $C_{mx\beta}$

c) Yawing moment derivative $C_{mz\beta}$

FIG 6. Comparison of the steady aerodynamic derivatives of the SG-VT configuration from different data sources for selected freestream conditions.

a) Pitching moment coefficient from the pitching motion for
$\alpha_0 = 0°$ and $\beta_0 = 0°$

b) Pitching moment coefficient from the pitching motion for
$\alpha_0 = 16°$ and $\beta_0 = 8°$

c) Yawing moment coefficient from the yawing motion for
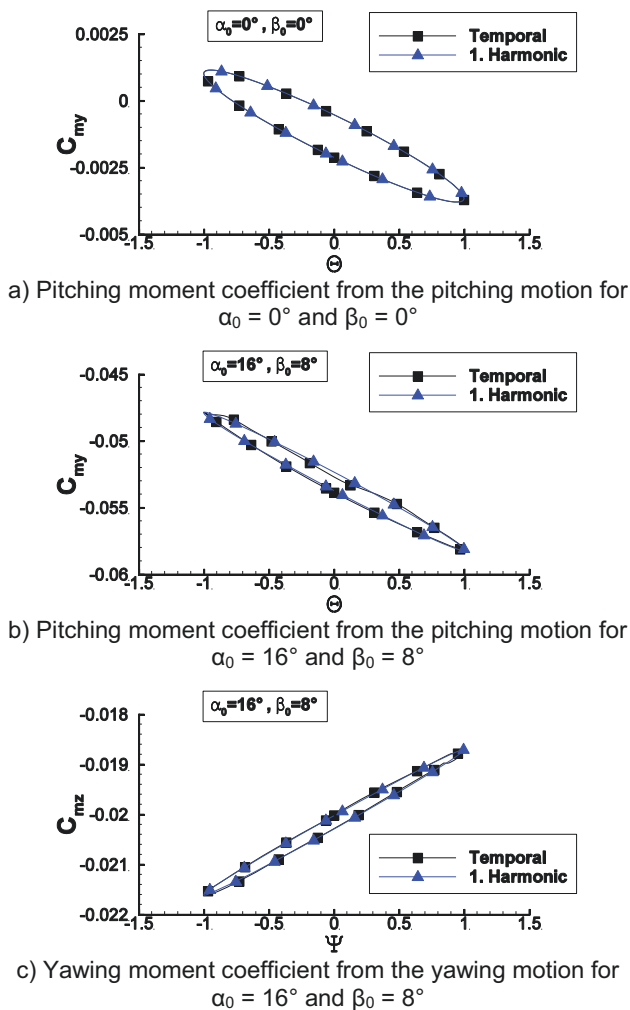$\alpha_0 = 16°$ and $\beta_0 = 8°$

FIG 7.　Lissajous figures for the pitching and yawing moment coefficient of the SG-VT configuration obtained by the temporal distribution of the aerodynamic coefficient and by the first harmonic of the corresponding aerodynamic coefficient for selected freestream conditions.

The applied approach furthermore requires linear characteristics with respect to the reduced frequency k. Linear characteristics are assumed to be met for moderate reduced frequencies of approximately k less than 0.2. The linear characteristics can be checked via the imaginary part of the first harmonic of the pitching moment coefficient, since the imaginary part represents the dynamics of the harmonic response. Considering the pitching motion, the requirements with respect to the reduced frequency are met, if the imaginary part of the coefficient shows linear characteristics and becomes zero for a reduced frequency of k = 0. Figure 8 illustrates the first harmonics of the pitching moment coefficient of the SG-VT configuration for a freestream condition of $\alpha_0 = 0°$ and $\beta_0 = 0°$ versus the reduced frequency k. Three different reduced frequencies of k = 0.05, k = 0.1 and k = 0.2 are simulated. The imaginary part representing the dynamics of the aerodynamic response shows linear characteristics with respect to the reduced frequency and shows a trend approaching a value of zero for a zero reduced frequency. The real part, which is used to determine the steady derivative, is constant over the considered reduced frequency. Consequently, the

dynamic motion has no influence on the quasi-steady part of the solution at the considered freestream condition. The first harmonics of the pitching moment coefficient demonstrate that the requirements associated to linear characteristics with respect to the reduced frequency of the applied approach are met. Consequently, the applied reduced frequency and excitation angles are chosen appropriately in order to apply the presented calculation method for the dynamic derivatives.
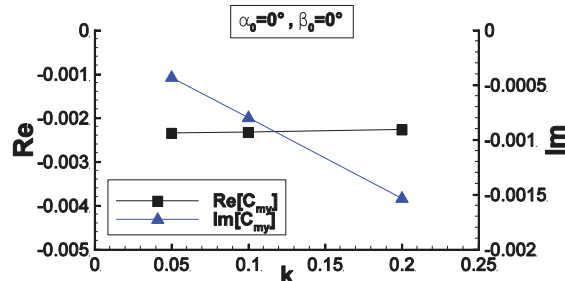

FIG 8.　First Harmonics of the pitching moment coefficient versus the reduced frequency due to pitching motion of the SG-VT configuration for $\alpha_0 = 0°$ and $\beta_0 = 0°$.

5.2.　Damping Derivatives

The damping derivatives associated with the pitching and yawing motion are coupled derivatives, since these motions are a combination of several degrees of freedom. They are determined via the harmonic aerodynamic response to the forced harmonic oscillations of the rigid aircraft. The damping derivative of the pitching motion reads $C_{my\dot{\alpha}} + C_{myq}$ and the damping derivative associated with the yawing motion is $C_{mzr} - C_{mz\dot{\beta}} \cos\alpha_0$. This formulation also accounts for initial freestream conditions with $\alpha_0 \neq 0°$ and $\beta_0 \neq 0°$. Considering an increasing angle of attack α_0 and/or sideslip angle β_0, the cross and cross-coupling derivatives become important as well, which are, however, not subject of this paper.
The damping derivatives are determined for the SAGITTA configuration SG-00 without double V/T and SG-VT with attached double V/T. A statement about the dynamic stability of the SAGITTA configuration can be made by means of the sign of the corresponding damping derivative.

5.2.1.　Pitch-Damping Derivative

Figure 9 shows the pitch-damping derivative of the SG-VT and the SG-00 configuration for the considered angle of attack and sideslip angle range as well as a comparison of both configurations for selected freestream conditions. A negative pitch-damping derivative represents dynamically stable characteristics. Considering a dynamically increasing angle of attack, the dynamic effect induces a negative pitching moment, which represents a stabilizing nose-down pitching moment.
The SG-00 configuration shows dynamically stable characteristics for all considered freestream conditions, see Figure 9a. This is observed by means of the consistently negative pitch-damping values. Non-linear characteristics with respect to the angle of attack are observed for a zero sideslip angle. Of special interest is the freestream condition at $\alpha_0 = 8°$ and $\beta_0 = 0°$, since the gradient of the pitch-damping derivative switches its sign.

a) Pitch-damping derivative of the SG-00 configuration

b) Pitch-damping derivative of the SG-VT configuration

c) Pitch-damping derivative and its composition for both configurations for $\beta_0 = 0°$

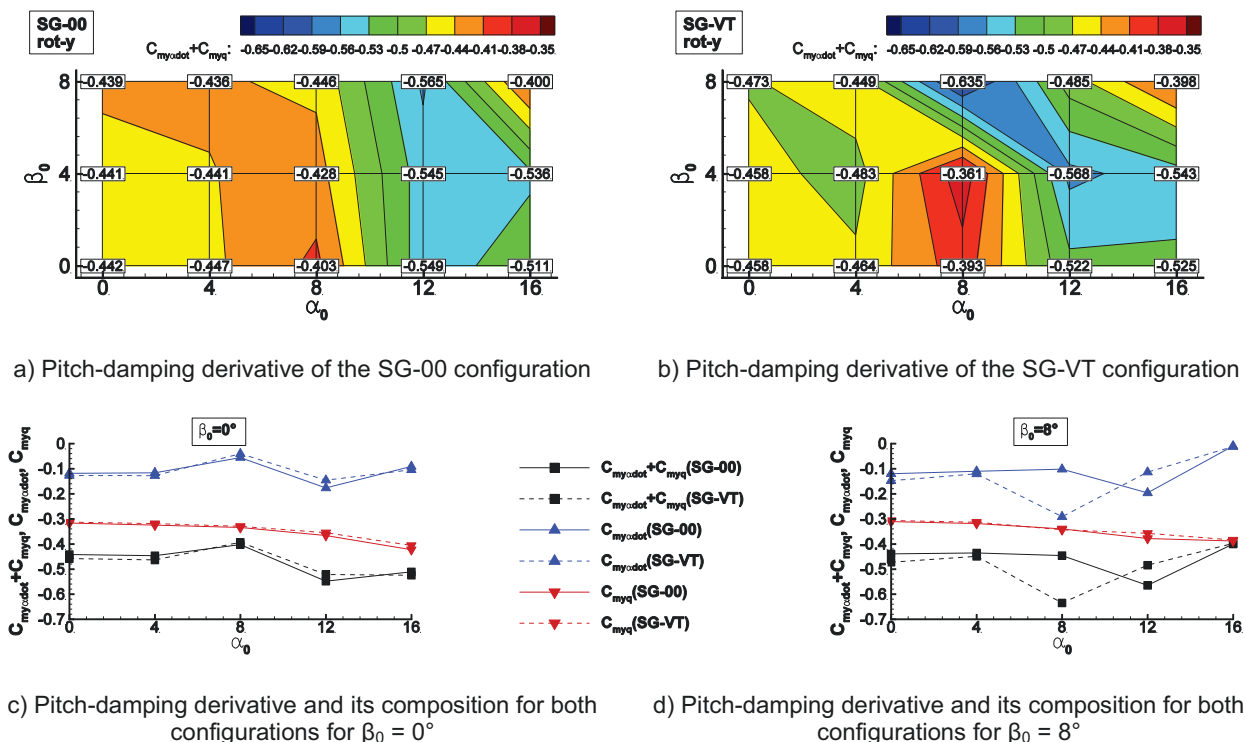d) Pitch-damping derivative and its composition for both configurations for $\beta_0 = 8°$

FIG 9. Pitch-damping derivative of the SG-00 and the SG-VT configuration over the considered angle of attack and sideslip angle regime and a comparison of both configurations for selected freestream conditions.

Up to an angle of attack of $\alpha_0 < 8°$ the flow field is dominated by attached flow and the dynamic derivatives are almost independent of the angle of attack. For an angle of attack of $\alpha_0 \approx 8°$, the flow starts to separate at the outboard wing region, see Ref. [7]. The flow separation is very sensitive to changes of the freestream conditions and grows with increasing angle of attack. For $\alpha_0 = 8°$, where the flow separation is present, the pitching motion induces surface pressure levels at the outboard trailing-edge section resulting in a destabilizing pitching moment. However, with increasing angle of attack and area of irregular flow at the outboard region, the effect is reversed. The induced pressure levels at the flow separation region then entail a stabilizing pitching moment. Since this effect generally occurs in the same way for sideslip angles of $\beta_0 \neq 0°$, the pitch-damping derivatives do not change significantly with respect to the sideslip angle. For an angle of attack of $\alpha_0 = 16°$ and $\beta_0 = 8°$, however, the flow field considerably changes at the wing leeward side. At the outboard section the separated flow forms a second leading-edge vortex, evolving from the blunt leading edge, see Ref. [7]. The evolution of the leading-edge vortex at the blunt leading edge is very sensitive to varying freestream conditions. The induced pressure levels in consequence of the pitching motion are high and destabilize the configuration.

The pitch-damping derivative of the SG-VT configuration with attached double V/T is illustrated in FIG 9b. The SG-VT configuration is dynamically stable for all considered freestream conditions. The SG-VT configuration features the same pitch-damping characteristics as the SG-00 configuration at moderate angles of attack. Furthermore, no significant deviations between the pitch-damping derivatives are observed for the considered angle-of-attack polar for $\beta_0 = 0°$. The flow separation at the wing outboard section for $\alpha_0 \geq 8°$ as well as the additional evolving vortex at the leeward outboard section for $\alpha_0 = 16°$ and $\beta_0 = 8°$ are present. For $\alpha_0 \geq 8°$ and $\beta_0 \geq 4°$, however, the effects of the double V/T additionally influence the pitch-damping derivatives. At $\alpha_0 = 8°$ and $\beta_0 = 8°$, a significantly increased pitch-damping stability is present in comparison to adjacent points. For this freestream condition, a leading-edge vortex is present at the leeward side of the windward vertical tail, see Ref. [7]. The pitching motion affects the sensitive flow around the vertical tail and induces a negative surface pressure at the wing surface near the wing/vertical tail junction. The resulting induced pitching moment stabilizes the configuration. This effect decreases with increasing angle of attack.

In Figure 9c and Figure 9d the pitch-damping derivatives for the SG-00 and SG-VT configuration are compared to each other for $\beta_0 = 0°$ and $\beta_0 = 8°$, respectively. The separated parts of the pitch-damping derivative, $C_{my\dot{\alpha}}$ and C_{myq}, are illustrated as well. $C_{my\dot{\alpha}}$ is obtained by a harmonic analysis of a heave motion and C_{myq} is obtained by quasi-steady rotational motions about the pitch axis. The sum of both parts results in the pitch-damping derivative obtained by the oscillating pitch motion. For zero sideslip angle both configurations feature the same pitch-damping derivatives over the angle of attack range, see Figure 9c. The pitch-damping derivative of both configurations is composed of approximately $1/3 C_{my\dot{\alpha}} + 2/3 C_{myq}$. The non-linear characteristics observed in the pitch-damping derivative are mainly associated with the dynamic derivative $C_{my\dot{\alpha}}$ obtained by the harmonic heave oscillations. The C_{myq} derivative obtained by the quasi-steady rotational motions features almost linear characteristics. For $\beta_0 = 8°$, the pitch-damping derivative is

also composed of approximately $1/3C_{my\dot\alpha} + 2/3C_{myq}$ for most of the flight conditions. Since the C_{myq} derivative is almost the same for both configurations, the present deviations between the pitch-damping derivatives with respect to β_0 are associated with the $C_{my\dot\alpha}$ derivative. Furthermore, the non-linear characteristics of the pitch-damping derivative with respect to the angle of attack and sideslip angle are a result of the $C_{my\dot\alpha}$ part as well.

5.2.2. Yaw-Damping Derivative

The yaw-damping derivative for both considered SAGITTA configurations is presented in Figure 10. At first, the yaw-damping derivative of the SG-00 and SG-VT configuration are separately shown for the considered angle-of-attack range and sideslip angle range, see Figure 10a and Figure 10b. The SG-00 configuration shows almost constant values for all sideslip angles up to an angle of attack of $\alpha_0 = 8°$, see Figure 10a. For this flight range, the values are approximately zero and thus no yaw-damping is present. With increasing angle of attack, the yaw-damping derivatives increase non-linear. The significant increase of the yaw-damping derivative is mainly a result of the evolving flow separation in the outboard wing area. This area is very sensitive to varying flow conditions in consequence of the yaw motion. The induced surface pressures near the wing leading edge at the outboard wing section result in a destabilizing yawing moment. This effect strengthens with increasing angle of attack. A dependency on the sideslip angle is observed for $\beta_0 > 4°$. For $\alpha_0 = 16°$ and $\beta_0 = 8°$, the additional leading-edge vortex in the leeward outboard wing section has a considerably stabilizing effect on the yaw-damping characteristics. However, the yaw-damping characteristics for this freestream condition are still unstable.

Figure 10b illustrates the yaw-damping derivatives for the SG-VT configuration. The overall attached flow field results in almost constant yaw-damping derivatives for $\alpha_0 \leq 4°$ and all considered sideslip angles. The negative values indicate a stable yaw-damping behavior. Significant non-linearities are observed for all sideslip angles at higher angles of attack. Considering freestream conditions with $\beta_0 = 0°$, the double V/T generally shows a stabilizing effect since the yaw-damping derivatives are decreased in comparison to those of the SG-00 configuration. With increasing angle of attack, the stability, however, decreases for the same reasons described for the SG-00 configuration. The positive yaw-damping derivative indicates an unstable yaw damping at the maximum considered angle of attack. Considering freestream conditions with sideslip angles $\beta_0 \neq 0°$ and angles of attack $\alpha_0 \neq 0°$, a leading-edge vortex at the leeward side of the windward V/T evolves, cf. Ref. [7]. This leading-edge vortex is sensitive to the locally varying flow condition in consequence of the yawing motion and entails strong non-linear characteristics with respect to the sideslip angle and angle of attack. The yawing motion strengthens the leading-edge vortex at the windward V/T for $\alpha_0 = 8°$ and $\beta_0 = 8°$, which results in reduced surface pressure coefficients and a destabilizing yawing moment. This effect is represented by a considerable increased yaw-damping derivative. With increasing angle of attack, however, this effect is reversed. The yawing motion weakens the leading-edge vortex at the leeward side of the V/T. This entails increased surface pressure coefficients and a stabilizing yawing moment.

In Figure 10c, the yaw-damping derivative and its composition versus the angle of attack is shown for the SG-00 and the SG-VT configuration at $\beta_0 = 0°$. The yaw-damping characteristics of both configurations are very similar with a certain offset between the values of both configurations.
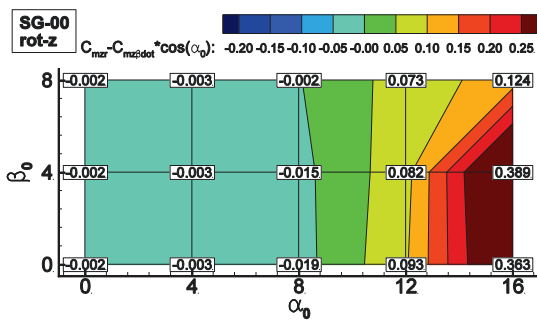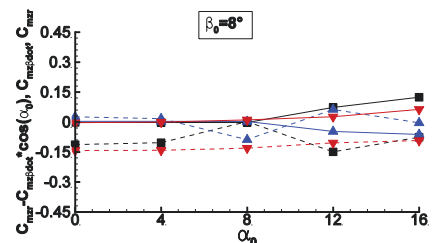

a) Yaw-damping derivative of the SG-00 configuration
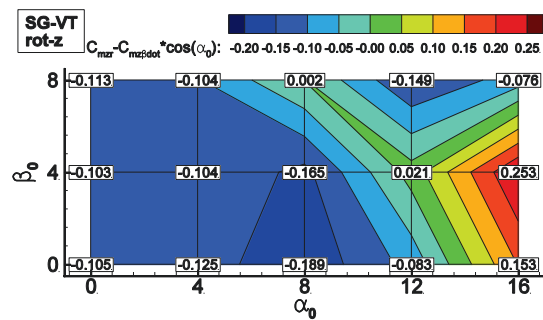
b) Yaw-damping derivative of the SG-VT configuration
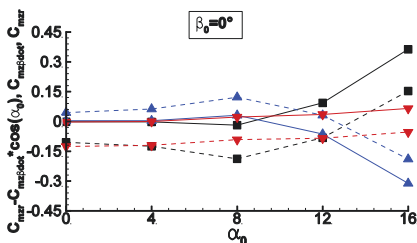
c) Yaw-damping derivative and its composition for both configurations for $\beta_0 = 0°$

d) Yaw-damping derivative and its composition for both configurations for $\beta_0 = 8°$

FIG 10. Yaw-damping derivative of the SG-00 and the SG-VT configuration over the considered angle of attack and sideslip angle regime and a comparison of both configurations for selected freestream conditions.

The attached double V/T significantly increases the stability of the configuration without introducing additional non-linearities. The yaw-damping derivative is decomposed in its parts C_{mzr} and $C_{mz\dot{\beta}}$. C_{mzr} is obtained by quasi-steady rotational motions about the yawing axis and $C_{mz\dot{\beta}}$ is obtained by harmonic lateral oscillations. It is observed that the non-linear effects for $\alpha_0 > 4°$ are mainly introduced by the $C_{mz\dot{\beta}}$ derivative. In case of the SG-00 configuration, both parts feature values of approximately zero up to $\alpha_0 = 4°$. With increasing angle of attack, the $C_{mz\dot{\beta}}$ derivative considerably increases, whereas the quasi-steady C_{mzr} derivative is almost constant with respect to the angle of attack. Considering the SG-VT configuration, the quasi-steady C_{mzr} derivative shows negative values, which are slightly increasing with respect to α_0. The non-linear effects are mainly introduced by the $C_{mz\dot{\beta}}$ derivative. With increasing angle of attack, the derivative decreases with strong non-linear characteristics. The sideslip angle of $\beta_0 = 8°$ is considered in Figure 10d. The yaw-damping derivatives for the SG-00 configuration feature less distinct non-linearities for this sideslip angle. The evolving leading-edge vortex at the leeward outboard wing section considerably enhances the yaw-damping characteristics at high angles of attack. Since the quasi-steady derivative C_{mzr} does not significantly change with respect to the sideslip angle, the additional leading-edge vortex mainly influences the $C_{mz\dot{\beta}}$ derivative. Considering the SG-VT configuration, the variation of the sideslip angle mainly affects the $C_{mz\dot{\beta}}$ derivative. The yaw-damping for $\beta_0 = 8°$ is mainly ensured by the quasi-steady C_{mzr} derivative, whereas the $C_{mz\dot{\beta}}$ derivative fluctuates around the zero value with respect to the angle of attack.

6. CONCLUSION AND OUTLOOK

This paper has presented results of numerical investigations of some unsteady aerodynamic characteristics of the SAGITTA diamond-wing configuration at low-speed wind tunnel conditions. The investigations have been conducted for the SAGITTA configuration with attached double vertical tail (V/T) and without double V/T at several angles of attack and sideslip angles. The pitching and yawing derivatives have been determined by means of the aerodynamic response to forced harmonic pitch and yaw oscillations, respectively. In order to evaluate the calculation methodology of the applied approach, steady aerodynamic derivatives available from the dynamic CFD simulations have been compared to steady aerodynamic derivatives available from steady CFD simulations and steady wind tunnel experiments. Furthermore, the absence of higher harmonics and the linear characteristics with respect to the reduced frequency have been checked. The results proof the compliance of the restrictions and substantiate the application of the described calculation methodology.

The pitch-damping derivative $C_{my\dot{\alpha}} + C_{myq}$ resulting from the pitch oscillations shows dynamically stable characteristics at all considered freestream conditions and for both SAGITTA configurations. The attached double vertical tail influences the pitch-damping derivatives for a sideslip angle of $\beta_0 \neq 0°$. Depending on the freestream condition the double V/T increases or decreases the dynamic stability in comparison with the clean configuration. Non-linear characteristics of the pitch-damping derivative are observed with respect to the angle of attack and sideslip angle. The non-linear effects stem

from the $C_{my\dot{\alpha}}$ part of the pitch-damping derivative, whereas the quasi-steady C_{myq} derivative reveals linear characteristics.

The yaw-damping characteristics are much more critical than the pitch-damping characteristics. Without double V/T the yaw-damping derivative $C_{mzr} - C_{mz\dot{\beta}}$ indicates considerable unstable yaw-damping behavior for increasing angles of attack and sideslip angles. The attached double V/T entails a significant improvement of the yaw damping behavior for the majority of the considered freestream conditions. Considering increasing angles of attack and sideslip angles, the yaw-damping characteristics with respect to the angle of attack and sideslip angle feature significant non-linearities. Those non-linearities can be associated with the $C_{mz\dot{\beta}}$ derivative. In contrast, the quasi-steady C_{mzr} derivative features linear characteristics with respect to the angle of attack and only weak dependencies on the sideslip angle. For $\beta_0 > 0°$, the quasi-steady C_{mzr} derivative mainly ensures the lateral stability of the SG-VT configuration.

In general, the considered damping derivatives show a constant distribution at moderate freestream conditions. Increasing the angle of attack and sideslip angle, results in significant non-linear characteristics of the damping derivatives. The non-linearities indicate that approaches using linear aerodynamic theory are not an appropriate tool to determine the dynamic derivatives, especially at higher angle of attacks and sideslip angles. In order to understand the non-linear effects observed in the results, further investigations, exploiting, e.g., harmonic surface pressure distributions and flow field visualizations, are necessary.

ACKNOWLEDGEMENTS

REFERENCES

[1] Breitsamter, C.: Turbulente Strömungsstrukturen an Flugzeugkonfigurationen mit Vorderkantenwirbeln, Dissertation, Technische Universität München, Herbert Utz Verlag, ISBN 3-89675-201-4, 1997.

[2] Gursul, U.: Review of Unsteady Vortex Flows over Slender Delta Wings, J Aircraft 42 (2) (2005) 299-319.

[3] Hummel, D.: On the Vortex Formation over a Slender Wing at Large Angles of Incidence, In: AGARD Specialists' Meeting on "High Angle of Attack Aerodynamics", Sandefjord, Norway, October 4-6, 1978, No. 247 in AGARD Conference Proceedings, pp. 15-1 – 15-17.

[4] Hövelmann, A.; Breitsamter, C.: Leading-Edge Geometry Effects on the Vortex Formation of a Diamond-Wing Configuration, J Aircraft 52 (5) (2015) 1596-1610.

[5] Hövelmann, A; Grawunder, M.; Buzica, A.: Breitsamter, C.: AVT-183 Diamond Wing Flow Field Characteristics Part 2: Experimental Analysis of Leading-Edge Vortex Formation and Progression; Aerosp. Sci. Technol., 2015, Article in press; DOI: 10.106/j.ast.2015.12.023.

[6] Hövelmann, A., Knoth, F.; Breitsamter, C.: AVT-183 Diamond Wing Flow Field Characteristics Part 1: Varying Leading-Edge Roughness and the Effects on Flow Separation Onset; Aerosp. Sci. Technol., 2015, Article in press; DOI: 10.106/j.ast.2016.01.002.

[7] Hövelmann, A.; Pfnür, S.; Breitsamter, C.: Flap Efficiency Analysis for the SAGITTA Diamond Wing Demonstrator Configuration; CEAS Aeronautical Journal, Vol. 6, No. 4, pp. 498-514, 2015.

[8] Schütte, A.; Hummel, D.; Hitzel, S.: Flow Physics Analysis of a Generic Unmanned Combat Aerial Vehicle Configuration; J Aircraft 49(6), 2012, pp. 1638-1651.

[9] Vicroy, D.D.; Loeser, T.D.; Schütte, A.: Static and Forced-Oscillation Tests of a Generic Unmanned Combat Air Vehicle, J Aircraft 49(6), pp. 1558-1583, 2012.

[10] Bryan, G.H.: Stability in Aviation, Macmillan, London, 1911, pp. 19-37.

[11] Pamadi, N.B.: Performance, Stability, Dynamics, and Control of Airplanes, 2nd ed., AIAA Education Series, AIAA, Reston, VA, 2004.

[12] Orlik-Rückemann, K.J.: Effect of High Angles of Attack on Dynamic Stability Parameters; In: AGARD Specialists' Meeting on "High Angle of Attack Aerodynamics", Sandefjord, Norway, October 4-6, 1978, No. 247 in AGARD Conference Proceedings, pp. 1-1 – 1-14.

[13] Da Ronch, A.; McCracken, A.J.; Badcock, K.J.; Widhalm, M.; Campobasso, M.S.: Linear Frequency Domain and Harmonic Balance Predictions of Dynamic Derivatives. J Aircraft 50(3), pp. 694-707, 2013.

[14] Da Ronch, A.; Vallespin, D.; Ghoreyshi, M.; Badcock, D.J.: Evaluation of Dynamic Derivatives Using Computational Fluid Dynamics. AIAA J 50(2), pp. 470-484, 2012.

[15] Förster, M.; Fleischer, D.; Breitsamter, C.: Computation of Unsteady Aerodynamic Derivatives Using a Small Disturbance Euler-/Navier-Stokes-Method. In: Assessment of Stability and Control Prediction Methods for NATO Air and Sea Vehicles Meeting Proceedings, RTO-MP-AVT-189, 2011.

[16] Rohlf, D.; Schmidt, S.; Irving, J.: Stability and Control Analysis for an Unmanned Aircraft Configuration Using System-Identification Techniques; J Aircraft 49(6), pp. 1597-1609, 2012.

[17] Loeser, T.; Rohlf, T.: Experimental Determination of Dynamic Derivatives in a Wind Tunnel Using Parameter Identification; Contributions to the 19th STAB/DGLR Symposium Munich, Germany, 2014, pp. 651-662.

[18] Seifert, J.: SAGITTA – Nationale Forschungskooperation für fortschrittliche UAV-Technologien im Rahmen der Open Innovation Initiative von Cassidian; 61st Deutscher Luft- und Raumfahrtkongress, Berlin, Germany, September 10-12, 2012, No. 1352 in DLRK 2012.

[19] Gerhold, T.: Overview of the hybrid RANS code TAU. In: MEGAFLOW-Numerical Flow Simulation for Aircraft Design, Vol. 89 of Notes on Numerical Fluid Mechanics and Multidisciplinary Design, pp. 81-92, Springer Verlag, 2005.

[20] Schwamborn, D., Gerhold, T., Heinrich, R.: The DLR TAU-Code: Recent Applications in Research and Industry. In: 4th European Conference on Computational Fluid Dynamics (ECCOMAS CFD 2006), Egmond aan Zee, The Netherlands, 2006.

[21] Fritz, W., Davis, M.B., Karman, S.L., Michal, T.: Reynolds-Averaged Navier-Stokes Solutions for the CAWAPI F-16XL Using Different Hybrid Grids. J Aircraft 46(2), 409-422, 2009.

[22] Jameson, A., Schmidt, W., Turkel, E.: Numerical Solutions of the Euler Equations by Finite Volume Methods using Runge-Kutta Time Stepping Schemes. In: 14th AIAA Fluid and Plasma Dynamics Conference, Palo Alto (CA), United States, No. 1259 in AIAA, 1981.

[23] Turkel, E.: Improving the Accuracy of Central Difference Schemes. NASA CR 181712, 1988.

[24] Jameson, A., Yoon, S.: Lower-Upper Implicit Schemes with Multiple Grids for the Euler Equations. AIAA J 25(7), 929-935, 1987.

[25] Spalart, P. R., Allmaras, S. R.: A One-Equation Turbulence Model for Aerodynamic Flows. In: 30th Aerospace Sciences Meeting & Exhibit, Reno, United States, No. 0439 in AIAA, 1992.

[26] Allmaras, S. R., Johnson, F. T., Spalart, P. R.: Modifications and Clarifications for the Implementation of the Spalart-Allmaras Turbulence Model. In: 7th International Conference on Computational Fluid Dynamics (ICCFD7), Big Island (HI), United States, 2012.

[27] Schütte, A., Boelens, O.J., Oehlke, M., Jirasek, A., Löser, T.: Prediction of the Flow Around the X-31 Aircraft Using Three Different CFD Methods. Aerosp. Sci. Technol. 20(1), 21-37, 2012.